Journal of Molecular Structure 1327 (2025) 141192

Contents lists available at ScienceDirect

Journal of Molecular Structure

journal homepage: www.elsevier.com/locate/molstr

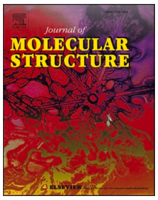

Combined experimental and computational studies of N-Phenyl-*o*-benzenedisulfonimide: Spectroscopy, DFT calculations, and Druggability analysis

Sedat Gumus [a,*], Mohammad Sadegh Sadeghi Googheri [b,c], Ahmet Gokhan Kazan [a], Bilge Eren [d]

[a] *Department of Physics, Faculty of Science, Ondokuz Mayis University, Samsun 55139, Turkey*
[b] *Instituto de Investigación Interdisciplinaria (I3), Vicerrectoría Académica, Universidad de Talca, 1 Poniente 1141, Talca, Chile*
[c] *Center for Bioinformatics, Simulation and Modeling (CBSM), Faculty of Engineering, Universidad de Talca, 1 Poniente 1141, 3466706, Talca, Chile*
[d] *Department of Chemistry, Faculty of Science, Bilecik Seyh Edebali University, Bilecik, 11210, Turkey*

ARTICLE INFO

Keywords:
Disulfonimide characterization
Spectroscopic analyses
DFT calculations
MD simulations
Enzyme inhibition

ABSTRACT

In this study, spectroscopic analyses and density functional theory (DFT) calculations have been used to characterize the N-phenyl-*o*-benzenedisulfonimide as a disulfonimide. Vibrational analysis using normal coordinate treatment revealed vibrational modes in the mid-IR and far-IR ranges, with an RMS error of 11.8 cm^{-1}. Diagnostic sulfonyl stretching vibrations were observed at 1345 cm^{-1} and 1325 cm^{-1} for the asymmetric modes, and at 1180, 1146 (s), and 1113 cm^{-1} in the IR spectrum. The ^{13}C and ^{1}HNMR spectra were recorded in DMSO, and chemical shifts were calculated at different levels of theories with the CPCM solvation model. It was found that the B3LYP/cc-pVTZ level of theory provided the best agreement between experimental and theoretical chemical shifts for both ^{13}C and ^{1}**H**NMR spectra in DMSO. X-ray crystallography revealed four intermolecular C-H···O hydrogen bonds in the crystal structure, which was further refined with the NoSpherA2 quantum chemistry method for enhanced accuracy. UV–Vis's analyses in both DMSO and chloroform solvents indicated predominant $\pi \rightarrow \pi^*$ transitions between benzene rings, which was further supported by the significant electron delocalization energies (10–30 kcal/mol) observed in the NBO analyses. Druggability analysis, including target prediction, molecular docking, MD simulations, and ADMET analysis, also identified the binding potential, stability, and pharmacokinetic properties of the title molecule. Notably, docking and MD simulations demonstrated selective inhibition of the CA XII enzyme, highlighting its potential as a promising candidate for developing new cancer therapies. Theoretical insights into local reactivity descriptors revealed the critical role of electronic properties in modulating enzyme-ligand interactions and the compound's inhibitory activity.

1. Introduction

Disulfonimides are organic compounds comprising two groups of sulfonyl at different points of the molecular structure and are also primary substances for antibiotic drugs known as sulfa drugs. Also, cyclic sulfonimides called sultams are well-known compounds in medicine. The sultams are the sulfonyl analogues of lactam antibiotics like penicillin [1,2]. In addition, sulfonimide derivatives such as acetazolamide, methazolamide, and dorzolamide are used in therapy of ulcers, epilepsy, gulaucoma, and some heart diseases as inhibitors of carbonic anhidraz [3,4]. Many researchers have recently studied intensively on inhibiting behaviors of carbonic anhydrase (CA) for sulfonamides, exhibiting powerful inhibitic features as well as antitumor activities as they attach together with more than one atom to enzymes [5–8].

CAs are a family of zinc metalloenzymes [6] that play a crucial role in regulating pH balance in various tissues. Among identified isoforms, CA XII has emerged as a promising target for cancer therapy due to its overexpression in several aggressive tumors. CA XII is often upregulated in cancers like renal cell carcinoma, glioblastoma, and melanoma [9–11]. This increased activity is linked to tumor growth, invasion, and resistance to therapy. Unlike other CA isoforms, CA XII is primarily located on the cell membrane, making it more accessible for targeted

---

* Corresponding author.
E-mail address: sedatg@omu.edu.tr (S. Gumus).

https://doi.org/10.1016/j.molstruc.2024.141192
Received 17 September 2024; Received in revised form 3 December 2024; Accepted 21 December 2024
Available online 22 December 2024

drug delivery [9,12,13]. Tumors often have an acidic environment, and CA XII helps cancer cells adapt and thrive in these conditions. Inhibiting CA XII can disrupt this adaptation and hinder tumor progression, and its selective inhibition holds significant promise for developing novel cancer therapies [14–16]. In contrast, CA II is abundantly expressed in normal tissues, and its inhibition can lead to side effects such as diuresis, electrolyte imbalance, and vision problems. Therefore, the ability of inhibitors to selectively bind CA XII over CA II is crucial for developing safer and more effective cancer treatments with fewer side effects.

Furthermore, disulfonimides have the ability to form metal complexes and metal salts with transition metals by assisting their ionizable groups (-NH and -SO_2) [17]. In analytical chemistry, they were extensively used to extract Cu, Cd, Co, Ni, and some alkali metals using a solvent. They were also used to find their complexes based on chiral derivatives [18] that act as catalysts [19] in their own asymmetric synthesis. Additionally, they serve as reactive agents in a variety of reactions due to separating very well to anion groups. N-Phenyl-o-benzenedisulfonimide (the title molecule) has been synthesized and investigated by one of the co-authors [20] to evaluate its hydrolysis kinetics and structure-reactivity relationship. It is an organic compound that belongs to the disulfonimide family (Fig. 1(a)). Therefore, it is crucial to clarify some of its structural characteristics through computational chemistry.

On the other hand, density functional theory (DFT) in computational studies has emerged as a powerful tool for investigating the molecular structure and vibrational spectrum of organic compounds, as well as UV-vis and NMR (^{13}C and ^{1}H) spectra. The x-ray data (with NoSpherA2 refinement), infrared and Raman spectra, and vibrational analysis of the compound in question were all reported in this work. The data was processed in normal coordinates at the DFT (B3YP/6–31G(d)) level. Further, DFT studies here are conducted to reveal structural and bonding properties, reactivity features, NBO properties, electrostatic potential, UV-vis, and NMR (^{13}C and ^{1}H) spectra in comparison with the experiment.

In this study, we also assessed the druggability of the title molecule using advanced computational tools. Initially, we employed the SwissTargetPrediction tool to identify potential protein targets of the title molecule [21]. This ligand-based tool predicts interactions by analyzing similarities between the title molecule and known ligands of a broad array of protein targets, thus suggesting possible biological pathways the title molecule might influence. Following the target prediction, we assessed the inhibitory activity of the title molecule against these targets using a two-pronged approach: molecular docking and molecular dynamics (MD) simulations. Molecular docking provided initial insights into the possible binding interactions between the title molecule and the target enzyme's active site. Subsequently, MD simulations were conducted to evaluate the stability and dynamics of the enzyme-inhibitor complexes over time. Unlike static docking techniques, MD simulations take into account the solvent effects, offering a dynamic view of how the aqueous environment influences the binding stability and interaction patterns. This approach also allows us to observe the flexibility and conformational changes in the enzyme, which are crucial for understanding the real-world efficacy of potential drug candidates [22,23]. Finally, we evaluated the physicochemical properties, pharmacokinetics, efficacy, and safety profiles of the title molecule and compared these aspects to approved drugs listed in the DrugBank database, utilizing the ADMET-AI web service [24]. This service provides comprehensive data that helps predict how the title molecule stacks up against established benchmarks in drug development. By integrating these computational strategies, we gain a complete understanding of the druggability of the title molecule, providing a robust foundation for further experimental validation.

2. Experimantal and computational methods

2.1. X-ray diffraction analysis

A suitable crystal of the title compound obtained in chloroform was meticulously chosen, and data collection ensued using a Bruker APEX-II CCD diffractometer, operating under MoKα radiation (λ = 0.71073) at a temperature of 273.15 K. The crystal structure was elucidated employing the Olex2 software [25], utilizing the olex2.solve [24] program with Charge Flipping for initial structure determination [26]. The R1 value of the refinement was reduced to 0.337 by using Shelxl [27] compatible with Olex2. To improve the refinement better, the NoSphereA2 refinment [28,29] under the Olex2.1.5 software were done. Here, the

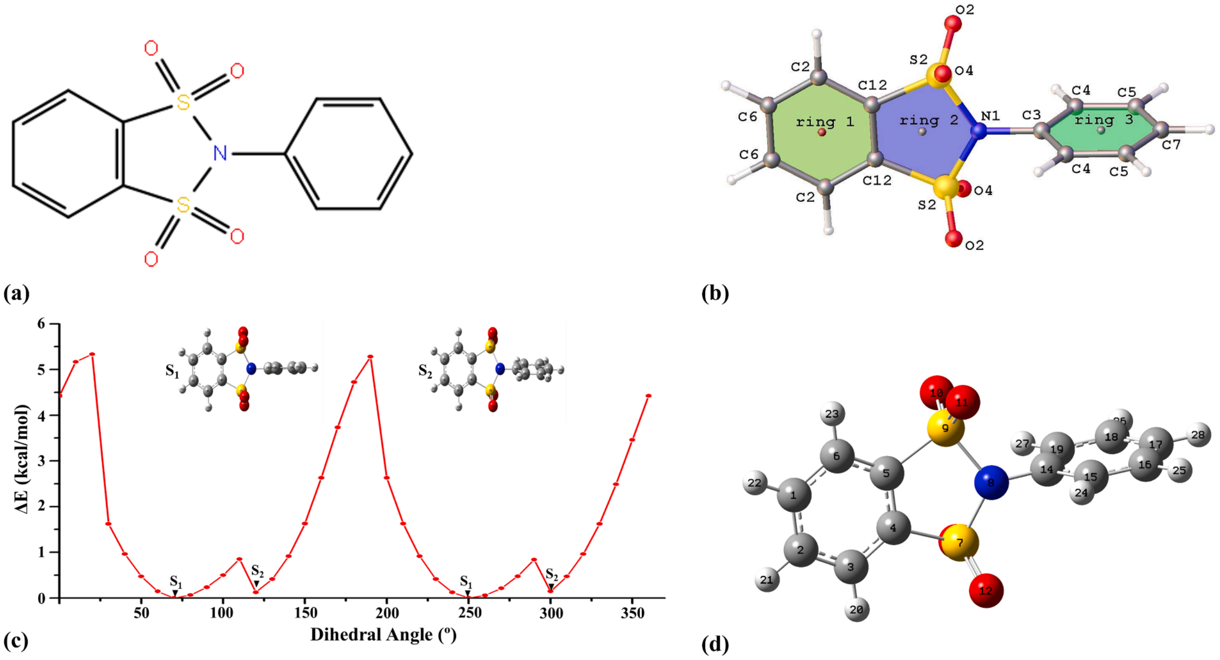

Fig. 1. The (a) structural formula, (b) crystal structure, and (c) optimized structure of the N-Phenyl-o-benzenedisulfonimide (title) compound. (d) One-dimensional potential energy surface around the S9-N8-C14-C19 dihedral angle.

NoSphereA2 refinement does not use a stardart structure refinement in which each atom interacts independently to others (IAM). However, this tool takes into account the intra- and inter molecular chemical bonding, which is referred to as the non spherical atomic electron density (or wave functions) for the non standart refinement. This electron density is needed to calculate non spherical atomic form factors, which are complex. The atomic electron densities or wave functions were calculated at the level of the theory PBE/def2-TZVPP implemented in the ORCA free software [30,31].

In the sake of this quantum mechanical crystallography refinement, both refinement is further improved and the atomic positions of hydrogens are as better as in the results of the neutron diffraction. The structure was successfully solved, with the space group unequivocally identified as C2/c, and finally, the refinement converged to R1= 0.0236. For a comprehensive understanding, detailed information regarding the crystal X-ray diffraction data and structure refinement for the title molecule is meticulously documented in Table 1. Access to crystallographic data is available upon request via the email address "data_request@ccdc.cam.ac.uk" with the CCDC number 2361583 to the Cambridge Crystallographic Data Center.

2.2. Infrared, Raman, NMR and UV–Vis measurements

FT-IR spectra of the title molecule were mesured in room temperature in the mid-IR region of 4000–400 cm^{-1} at a resolution of 1 cm^{-1} using a Bruker Vertex 80V FT-IR spectrometer. On the other hand, the far-IR region of 400–50 cm^{-1} was recorded in Perkin-Elmer FT-IR 2000 spectrometer at a resolution of 2 cm^{-1}. The samples used for mid-IR and far-IR measurements were KBr and polyethylene pellets, respectively. The Raman spectrum in the range 4000–60 cm^{-1} was also recorded at a resolution of 3cm^{-1} via Bruker Senterra Dispersive Raman Microscope using the 532 nm line of a 3B diode laser. ^{1H}NMR and ^{13C}NMR spectra were recorded with NMR spectrometer (Oxford-NMR300) using DMSO-d_6 as solvent. UV–Vis spectra were measured on a PG Instruments-T80 UV/VIS spectrometer in chloroform and DMSO.

2.3. Computational details

All the QM calculations were performed with DFT implemented in Gaussian16 software program [32]. Molecular geometrical optimization and also harmonic vibrational frequencies of the title molecule was carried out without any constraint to its geometry at the level of the same theory. No imaginary vibrational frequencies were in analytic second derivatives of potential energy surface (PES), indicating that molecule has a global minimum. Normal coordinate analysis was done with MOLVIB program [33,34]. Harmonic force constant matrix in Cartesian coordinates necessary for normal coordinate analysis were obtained at the level of B3LYP/6–31G(d). This program has ability of transforming force constants matrix from Cartesian to internal symmetry coordinates, scaling and also calculating PED values, IR and Raman intensities. Moreover, this program receives atomic coordinates, atomic masses, harmonic force constants and dipole derivatives belonging to an optimised molecule in gas phase as an input, which are extracted by the RDARCH program written by Sundius. Multi-scaling procedure in normal coordinate analysis is achieved with least squares method to catch the best agreement between observed frequencies and calculated ones. PED values above 10 % were acceptable for consideration.

Table 1
Crystal data and structure refinement for the title compound.

CCDC deposition number 2361583	
Empirical formula	$C_{12}H_9NO_4S_2$
Formula mass (g ·mol^{-1})	295.342
Temperature (K)	273.15
Crystal system	Monoclinic
Space group	C2/c
Crystal color	Colourless
Unit cell dimensions (a, b, c) (Å)	10.673(3), 13.148(4), 10.042(3)
Unit cell angles (α, β, γ)	90°, $116.547(8)^{\circ}$, 90°
Volume ($Å^3$)	1260.6(6)
Z	4
Density ρ(g/cm^{-3})	1.556
Absorption coefficient (μ/mm-1)	0.431
Absorption correction	Multi-scan
Radiation	MoK_{α} (λ = 0.71073)
Crystal size (mm^3)	0.1 × 0.09 × 0.05
F000	609.351
2θ range for data collection ($^{\circ}$)	5.28 to 53
Index ranges	$-14 \leq h \leq 14$, $-17 \leq k \leq 17$, $-13 \leq l \leq 13$
Reflections collected	11219
Independent reflections	1307 [R_{int} = 0.0399, R_{sigma} = 0.0262]
Data/restraints/parameters	1307/0/129
Goodness of fit on F2	1.087
Final R indexes [I≥2σ(I)]	R_1= 0.0236, wR_2= 0.0529
Final R indexes [all data]	R_1= 0.0311, wR_2= 0.0569
Largest difference peak hole (e/$Å^{-3}$)	0.26/-0.18

The Raman activities from Molvib program after completing scale procedure have been transformed to relative Raman intensities according to Raman scattering formula in [35]. The spectra were simulated using the SIMIRRA program [36], with Lorentzian line shapes and a full width at half maximum (FWHM) of 5 cm^{-1} employed. Natural Bond Orbital (NBO) Analysis was performed with NBO 7.0.10 [37] program to evaluate the donor-acceptor interactions in terms of the second order Fock Matrix based on NBO basis. The NMR GIAO calculations were conducted in a DMSO solvent medium using the conductor-like polarizable continuum model (CPCM) to ascertain the ^{1}H- and ^{13}CNMR chemical shifts. UVvis transitions were also done with the same solvation model. The global and local parameters (or descriptors) of chemical reactivity were estimated using the UCA-Fukui soft [38] by entering the log and fch files as an input from the Gaussian software.

The PDB structures of the target enzymes were obtained from the RCSB Protein Data Bank (https://www.rcsb.org) and water and ligand molecules were then removed from the structures. The enzymes and ligands were prepared for docking using AutoDock Tools [39]. For enzymes, all non-relevant molecules, including water and any co-crystallized ligands, were removed, while polar hydrogens and Kollman charges were added. Ligands were similarly pre-processed by adding Gasteiger charges, identifying rotatable bonds, and minimizing energy where necessary to ensure optimal flexibility during docking. AutoDock Vina 1.2.3 [40] was employed for docking calculations. The grid box, essential for defining the search space, was centered at the active site of each enzyme, covering the Zn(II) ion, a critical feature for CA activity. The grid box was carefully sized to 40 grid points in each dimension with a spacing of 0.375 Å between points, which allowed adequate coverage of the active site and ensured the ligand could explore all possible binding conformations. During the docking procedure, the ligands were allowed full flexibility, enabling them to explore different binding conformations, while the enzyme structures were treated as rigid. This rigid-body approach simplified the computational complexity while maintaining the structural integrity of the active site, particularly the coordination environment of the Zn(II) ion. The AutoDock Vina scoring function, which estimates binding free energy, was used to evaluate each binding pose generated. Ligand poses were grouped using a positional RMSD cutoff of 1.0 Å, ensuring that similar poses were clustered together. For each enzyme-ligand complex, the pose with the highest binding free energy (lowest score) within the top-ranked cluster was selected as the most probable binding configuration. Once docking was completed, the top-ranked binding pose for each complex was selected for further analysis, including visualization of interactions with key active site residues and the Zn(II) ion. The binding affinity, expressed as the predicted free energy, was recorded and compared across complexes. To investigate the most stable interactions, these poses were aligned with the receptor structure, allowing for a detailed examination of key ligand-receptor interactions. To ensure the reproducibility and reliability of the results, three independent simulations were performed for each system. This approach minimizes statistical errors and provides a more robust evaluation of the system's behavior by averaging the outcomes of multiple runs.

Following docking calculations, the enzyme-ligand complexes were used as initial inputs for MD simulations. Missing enzyme residues were reconstructed using Swiss-PdbViewer [41], and the Zn ion and crystallographic water molecules, essential for enzyme function, were kept. Simulations were performed with GROMACS 2022 [42], using the AMBER99SB force field [43] for enzymes and GAFF [44] for ligand topologies generated by ACPYPE [45]. The TIP3P water model [46] was employed, with systems neutralized and maintained at 0.15 M NaCl. After energy minimization, systems underwent gradual heating, followed by NVT and NPT equilibration at 310.15 K and 1 bar. Each system was then simulated for 100 ns under the NPT ensemble, with three replicates for reproducibility. The V-rescale thermostat [47] and Parrinello-Rahman barostat [48] were applied, with PME [49] for long-range electrostatics and LINCS [50] for bond constraints. Trajectories were saved every 10 ps with a 2-fs time step. Further details of the MD simulation setup and protocols can be found in the supporting information.

3. Results and discussion

3.1. *Conformal analysis and molecular geometry*

The title molecule given in Fig. 1(b) is an organic molecule contained 1,2-benzenedisulfonimide anion together with phenyl ring attached to its nitrogen atom, and has C_2 point group. The phenyl ring is chosen to find out the possible conformer of the title molecule and therefore, φ(S-

Table 2
Geometrical parameters of the title molecule.

	Bond length (Å)		
	B3LYP/6–31G(d)	X-Ray	Ref. [52]
C1-C2	1.399	1.386(3)	1.389(3)
C2-C3	1.397	1.3871(19)	1.393(2)
C3-C4	1.391	1.3820(16)	1.383(2)
C4-C5	1.39	1.382(2)	1.385(2)
N8-C14	1.442	1.4378(19)	-
C4-S7	1.789	1.7448(11)	1.7581(15)
S7-N8	1.737	1.6556(8)	1.6706(15)
S9-N8	1.737	1.6556(8)	1.6753(15)
S7-O12	1.459	1.4105(11)	1.4231(13)
S7-O13	1.463	1.4140(10)	1.4345(13)
C15-H24	1.084	1.072(17)	0.95
C19-H27	1.083	1.072(17)	0.95
C16-H25	1.086	1.071(17)	0.95
C17-H28	1.086	1.11(2)	0.95
C2-H21	1.085	1.072(17)	0.95
C3-H20	1.085	1.099(14)	0.95
	Bond Angle (°)		
	B3LYP/6–31G(d)	X-Ray	Ref. [52]
C2-C3-C4	118.07	117.89(13)	117.51(16)
C4-S7-N8	93.65	95.06(5)	97.31(7)
S7-C4-C3	123.54	123.72(9)	124.17(12)
C5-C4-S7	115.32	115.11	113.87(12)
C4-S7-O12	110.77	111.58(6)	113.19(8)
C4-S7-O13	110.05	110.99(6)	108.40(7)
N8-S7-O12	108.1	110.05(5)	108.24(8)
N8-S7-O13	111.58	109.56(5)	109.29(8)
C5-S9-O10	110.05	111.58(6)	109.23(8)
C5-S9-O11	110.77	110.99(6)	112.52(8)
N8-S9-O10	111.58	110.05(5)	109.67(8)
O12-S7-O13	119.61	117.34(7)	118.32(8)
N8-S9-O11	108.1	109.56(5)	107.50(8)
C3-C4-S7	123.54	123.72(9)	124.17(12)
C6-C5-S9	123.54	123.72(9)	124.86(13)
S7-N8-C14	117.77	120.17(4)	-
S7-N8-S9	114.38	119.65(8)	114.57(8)
C2-C3-H20	121.29	121.7(8)	121.24
C4-C3-H20	121.29	120.4(8)	121.252
C3-C2-H21	119.43	120.4(9)	119.62
	Dihedral Angle (°)		
	B3LYP/6–31G(d)	X-Ray	Ref. [52]
S7-N8-C14-C19	71.9	89.031	
C4-S7-N8-S9	-27.12	-0.18(5)	-17.18(11)
C14-N8-S9-O11	-74.82	-65.78(4)	-
C14-N8-S7-O13	-58.67	-65.78(4)	-
C14-N8-S7-O12	74.82	64.64(5)	-
C14-N8-S9-O10	58.67	64.64(5)	-
C14-N8-S9-C5	171.92	179.82(4)	-
C14-N8-S7-C4	-171.92	179.82(4)	-
C3-C4-C5-S9	-179.94	179.44(14)	-174.56(13)
C3-C4-C5-C6	0.00	-0.30(12)	0.2(3)
C3-C2-C1-C6	0.00	-0.66(17)	0.2(3)

N-C-C) torsional angle are varied from 0^0 to 360^0 at the steps of 10^0 by leaving all the geometrical parameters of the molecule relaxed along with the B3LYP/6–31G(d) calculations. We have encountered with two conformers S_1 and S_2 of the molecule reached to the local minimums at the torsional angles 0^0 and 360^0, respectively as noticed from Fig. 1(c). This result shows that our molecule has two possible molecular stuctures and their total energies are nearly equal to each other. In these two conformers, the phenyl ring has position perpendicular to the moiety “1,2-benzenedisulfonimide anion” [51]. The potential energy surface obtained here indicates that S_1 conformer is of more minimum energy. In this study, we based the most stable conformer on S_1.

Fig. 1(d) shows the molecular structure of S_1 conformer belonging to C_s point group symmetry after optimization. The optimized geometrical parameters have been calculated at the levels of B3LYP/6–31G(d). The optimised geometrical parameters were compared with the crystallogaphic data of the crystal structure of the title molecule and also the compound benzene-1,2-bis(sulfonyl)amine [52] in Table 2.

The optimised bond lengths, bond angles and dihedral angles of the title molecule are in agreement with the present crystal data and Ref. [52,53]. The optimised S=O bond length (the other S=O′) is 1.459 Å (1.463), while the corresponding crystal parameters are 1.4105(11) Å (1.4140(10)) and 1.4231(13) Å length (1.4345(13)) in [53]. The O=S=O angle was calculated to be 119.61^0 while the corresponding crystal values were measured to be $117.34(7)^0$ and $118.32(8)^0$ in [53]. The other crystal parameters such as C-N, C-S and C=C and C-S-N, C-C-S, C-S-O, N-S-O etc. seem to agree with the optimised values in Table 2. On the other hand, some calculated torsional bonds deviate slightly from the corresponding crystal values. However, the title molecule is not planar because the torsion angle of S_7-N_8-C_{14}-C_{19} is 71.9^0. The counterpart in the crystal data is 89.031^0. This appears to be the best configuration to alleviatate “steric congestion” of phenyl ring with the proximal sulfonyl protons. The mean reason of this angle deviation could be the present hydrogen bonds in the crystal structure in Table 3. Furthermore, there is no π-π stacking package in the monoclinic unit cell of the single crystal structure of the title molecule illustrated in Fig.2.

In addition, there are many studies in the literature on "benzene-1,2-disulfonyleamide anions" contained in salt and metal complexes. The geometrical parameters of these anions in the studies change from complex to complex because of their different coordinations so we may just present a rough comparison. The bond lengths S-N, S=O, C-S and C=C of the ring 2-moiety of the title molecule were calculated as 1.74 Å, 1.46 Å, 1.79 Å and 1.39 Å, respectively and these values are intermadiate with their corresponding ones of 1.56–1.60 Å, 1.43–1.44 Å, 1.75–1.78 Å, 1.38 Å as are in complexes of benzene-1,2-disulphonylimide anion.

3.2. NBO analysis

NBO analysis plays an effective role to study conjugation, hyperconjugation and charge transfers from the filled NBOs (Lewis-type orbitals or donors) to the unfilled NBOs (non-Lewis-type orbitals or acceptors). It provides insight into the character, hybridization, and order of a bond, the partial charges of each atom, and the dipole moment of a molecule. It also allows the estimation of potential resonance patterns and reactivity by examining the delocalized natural bond occupancy in a molecule and facilitates the understanding of spectroscopic study analysis [54,55].

Table S.1 shows effective second-order perturbation energies together with donor and acceptor NBOs, charge transfers between them, and also polarization coefficient and hybridization of each atomic centre in the NBO bond based as calculated by DFT-B3lyp/6–31G(d). It is seen from Table S.1 that a large electron delocalization exists in the title molecule. From conjugative point of view, this molecular system carries the strongest stabilization interactions of $\pi \rightarrow \pi*$on the ring 1 of the fused structure and on the ring 3. This interaction energies change between ~17–23 kcal/mol and contribute considerably to stabilization of this molecule. However, hyperconjugative interactions result in the charge transfers from lone pairs of oxygen atoms to vicinal antibonds such as $\sigma^*(C-S)$, $\sigma^*(N-S)$, and $\sigma^*(S-O)$. Their typical values are in between ~10–30 kcal/mol. Therefore, these important charge transfers to the antibonding natural orbitals influence to the equilibrium geometry of the molecule and weaken strengths of those σ bonds in question. It is well-known that bond strength is directly proportional to vibrational freqency. These larger energies show larger hyperconjugative and conjugative interactions between some donor and acceptor bonds of the molecular system. Here, we will not mention on the other hyperconjugations of$\sigma \rightarrow \sigma*$ due to their minor contributions but nevertheless chemically appreciable.

On the other hand, the central S atoms have ~sp^3d^0 hybridisation and the occupancy of the d orbitals is about 5 % [56]. For this reason, the sulphur atoms form tetrahedral bonds with the surrounding C, N and O atoms. The sulphur atoms require sp^3d^2 hybridisation to form hexavalency, but they do not show sufficient d-orbital occupancy to warrant d-orbital participation in hybrids. The NRT search of the title molecule confirms that the valence of the S atom is 3.77e, well below hexavalent (6e) and even slightly below tetravalent (4e). Furthermore, the oxygen atoms have valences of 1.31–1.43. They therefore have some double bond character (30–40 %), as O lone pairs delocalise into the relevant S-O, S-N and S-C anti-bonds. In other words, the electron density at S does not show a hypervalent character. Rather, each O has three lone pairs and only one bond to S. Thus, S is only tetravalent (two bonds to O atoms, one bond to N and one bond to C).

3.3. Molecular electrostatic potentials (MEP) and chemical reactivity analysis

Molecular electrostatic potential map conveys information about the charge distributions on a molecular system and is very useful to describe the reactive sites for electrophilic and nucleophilic attacks as well as noncovalent interactions [57] (hydrogen bonds, van der Walls forces etc.). Molecular electrostatic potential V(**r**) with the electronic charge density ρ(**r**) of a molecule are related according to Coulomb’s law,

$$V(r) = \sum_A \frac{Z_A}{|R_A - r|} - \int \frac{\rho(r')dr'}{|r' - r|}$$

and also, according to Poisson’s equation to each other,

$$\nabla^2 V(r) = 4\pi\rho(r) - 4\pi \sum_A Z_A \delta(r - R_A)$$

where Z_A is the charge on nucleus A located at $\mathbf{R}_A$, ρ(**r**) and V(**r**) are physical observables so that they are determined by diffraction

Table 3
Intermolecular hydrogen bond geometry in the singe crystal structure of the title compound.

D-H···A	(D-H)/Å	(H···A)/Å	(D···A)/Å	D-H···A/deg.	Symmetry Codes
C4-H4···$O4^1$	1.071(17)	2.473(18)	3.511(2)	162.87(13)	-x+1/2, -y+1/2, -z
C5-H5···$O2^1$	1.071(17)	2.596(18)	3.391(2)	130.47(13)	x,-y,+z-1/2
C6-H6···$O2^1$	1.071(17)	2.921(18)	3.398 (2)	107.32(13)	-x+1,-y+1,-z+1
C6-H6···$O4^1$	1.071(17)	2.383 (18)	3.391(2)	155.96 (13)	-x+1/2,+y+1/2,-z+1/2

D: Donor; **A**: Acceptor.

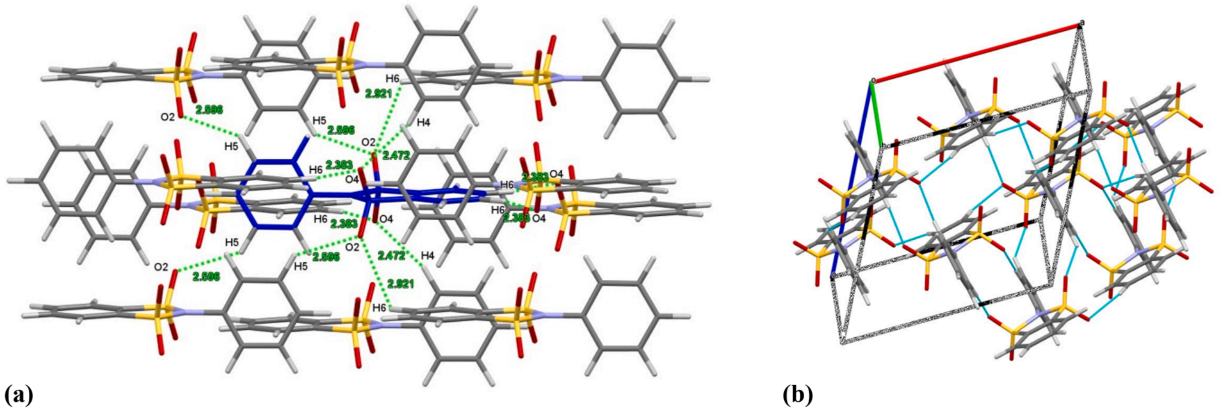

Fig 2. The analyzed intermolecular hydrogen bonding contacts of the title compound using Mercury 3.8 and WinGX v2014.1. The image clearly displays (a) the intermolecular interactions of the central blue molecule with the surrounding molecules and (b) the monoclinic unit cell of the single crystal structure of the title compound.

techniques as well as computationally. V(**r**) may be assumed as the potential of the molecule available on an electrical point charge at the point **r**. If this test point charge is positive, it will attract to regions of negative potential V(**r**) or it will be repelled from those regions of positive potential. The former leads to stabilization interaction energy, the latter to destabilization one.

In this study, MEPs were calculated in exact equilibrium geometry in order to predict these reactive sites and were plotted 3D isosurface of the title molecule taking the radial value for a particular electron density as ρ(**r**)=0.0004 a.u. surface, corresponding to 800 points on the isosurface. In Fig. 3, MEP predict the approximate size and shape of this molecular system where their maximum negative regions are qualitatively represented as red colour (-4.305e-2 a.u.), the maximum positive regions as blue one (+4.305e-2 a.u.) and intermediate ones with the other colours. Table S. 2 gives numerically MEP values and corresponding fit electrostatic charge for each atom in the title molecule. Red coloured regions show maximum electrostatic potentials V(**r**)=-58.9 a.u. and -22.3 a.u. over sulphur and oxigen atoms, respectively. These negative potential values indicate that the effect of the electrons predominates, and therefore are attractive to the approaching electrophile, representing electrophilic attack sites. Especially, the oxygen atoms here for this compound are candidates for intermolecular hydrogen bonds, as are in the crystal package of the title compound. On the other hand, the hydrogen atoms of the fused phenyl ring in the molecular system are illustrated with blue colour. In those regions which V(**r**) have positive values of *ca.* -1.06 a.u. are positive charge rich and therefore are relatively nucleophilic attack sites, in comparison with the atoms left.

Chemical reactivity is strongly influenced by the interaction between the frontier molecular orbitals (FMO), *i.e.*, the highest occupied molecular orbital (HOMO) and the lowest unoccupied molecular orbital (LUMO). The HOMO, rich in electron density, serves as the electron donor, while the LUMO, characterized by electron-deficient regions, acts as the electron acceptor. Small energy gaps between the HOMO of one species and the LUMO of another typically facilitate reactions. This concept helps explain the site selectivity and stereoselectivity observed in many organic and inorganic reactions, including nucleophilic and electrophilic attacks. Under Fukui's Frozen Orbital Approximation (FOA), this method provides a quantitative framework for calculating condensed Fukui functions for any atom (k-th atom). It does so by summing the products of the weighted orbital coefficients and the overlap integrals between the atomic basis functions and the atomic function associated with that atom within the framework of the FMO. In this study, the FMO method was employed to determine global and local reactivity parameters. The global reactivity parameters, calculated at the B3LYP/6–311++G(d,p) level using an ultrafine grid, are presented in Table 4. Here, the quantum mechanical descriptors for the global reactivity parameters, as outlined in Ref. [58], are consistent with those obtained using the UCA-Fukui software [38]. These include properties such as chemical potential (μ) and the electrophilicity index (ω), which describe the reactivity of the molecule as a whole. Fig. 3 displays the 3D HOMO-LUMO electron density maps of the title molecule. Based on the obtained results, the HOMO and LUMO of the title molecule are

Table 4
The calculated global reactivity parameters at the B3LYP/6–311++G(d,p) level of theory.

Parameters	(eV)
E_{HOMO}	-7.48
E_{LUMO}	-2.27
Ionization potential I	7.48
Electron affinity A	2.27
Energy gap	5.21
Electronegativity χ	4.88
Chemical potential μ	-4.88
Chemical hardness η	5.21
Chemical softness S	0.19 $(eV)^{-1}$
Electrophilicity index ω	2.29
Nucleophilicity index N	0.44

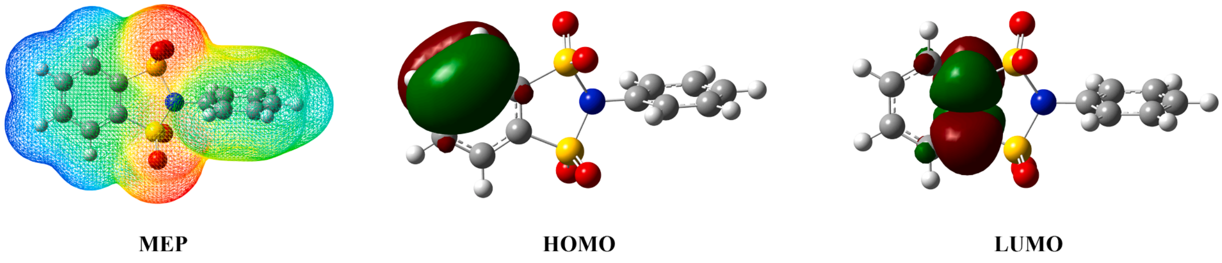

Fig. 3. Molecular potential surface (MEP) and frontier molecular orbitals (FMO) analysis of the title molecule.

predominantly composed of π and π^* orbitals associated with its phenyl ring. The HOMO demonstrates a π character of 73 % and a π^* character of 25 %, whereas the LUMO comprises 51 % π^* character and 13 % π character. The energy gap between the HOMO and LUMO is 5.21 eV. This relatively high value, as observed for the compounds discussed in Ref. [59], suggests that electron transfer between the frontier orbitals may be challenging. Consequently, this large gap suggests low chemical reactivity as well as high kinetic stability, meaning the compound is less likely to undergo reactions under typical conditions.

The descriptor ω is a quantitative measure of a ligand's electrophilicity. It is proportional to the square of the chemical potential (or electronegativity) and inversely proportional to the chemical hardness (η), providing insights into the molecule's ability to accept electrons. A compound becomes more reactive with a larger ω, lower η, and higher μ. For the title molecule, the global reactivity descriptors ω, μ, η and S were estimated to be 2.29 eV, -4.88 eV, 5.21 eV and 0.19 $(\text{eV})^{-1}$, respectively. The low S and high η values confirm that the molecule is relatively a hard molecule. However, the global electrophilicity index of 2.29 eV suggests a strong capacity to accept electrons, supporting the molecule's potential role in facilitating chemical reactions [60]. In addition, the low chemical potential of -4.88 eV supports the ability of the electron to accept. The positive hardness index of the title molecule shows its stability. Calculated local reactivity descriptors for each atom of the title molecule are given in Table S. 3. These descriptors indicate the reactivity of each atom in the molecule within the reaction mechanism. The f^-, f^+, and f^0 functions describe susceptibility to nucleophilic attack, electrophilic attack, and radical attack, respectively. The f^- values for the carbon atoms numbered 1, 2, 3, and 4 in the phenyl ring are 0.0936, 0.3813, 0.156, and 0.084, respectively, indicating that these atoms are potential sites for electrophilic attack. On the other hand, the f^+ values indicate that the almost skeletal structure of the title molecule serve as sites for nucleophilic attack. However, the -SO_2-N-SO_2 fragment is relatively more prone to nucleophilic attack, with condensed f+ indices for this fragment ranging from 0.0336 to 0.2291.

In particular, the sulfur atom appears to be a more favorable site for nucleophilic attack compared to the oxygen and nitrogen atoms. Radical attacks are distributed across the skeletal region, with a preference for the phenyl ring and the -SO_2-N-SO_2 fragment. On the other hand, the dual descriptor ($\Delta f = f^+ - f^-$) provides insights into site selectivity for nucleophilic or electrophilic attack. If $\Delta f > 0$, the site is more prone to nucleophilic attack; otherwise, it favors electrophilic attack. Based on this analysis, the phenyl ring is identified as the preferred site for

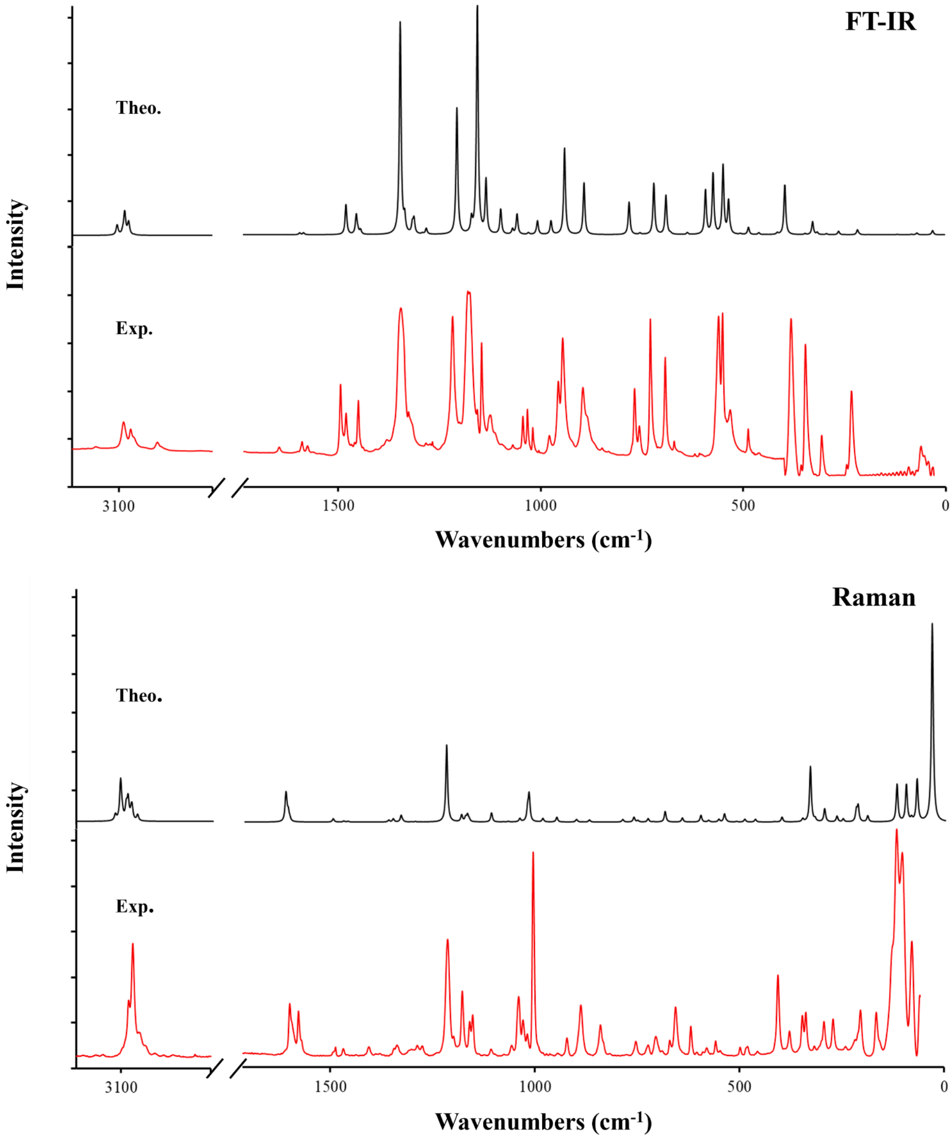

Fig. 4. Theoretical and experimental FT-IR and Raman spectra of the title molecule. Multi-scale factors were applied to the theoretical spectra.

electrophilic attack, whereas the -SO₂-N-SO₂ fragment is more suitable for nucleophilic attack. One of the oxygen atoms (O_{12}) has a dual descriptor value less than zero, indicating that it is an electrophilic attack site. This suggests the potential for forming a covalent bond with available nucleophilic sites. Other indices, such as local philicities, represent the electron-accepting power (ω^+) and electron-donating power (ω^-) of the title molecule. The condensed ω+ Fukui functions are effectively distributed across the skeletal structure of the molecule, with a predominance in the -SO_2-N-SO_2 fragment. Conversely, the condensed ω− Fukui functions are more concentrated in the phenyl ring region.

3.4. Assignment of vibrational bands

The assignment of the vibrational bands for FT-IR, FT-Raman characterization study has been performed with normal coordinate analysis for the title molecule. The present molecule belonging to Cs point group consists of 28 atoms, and has 78 fundamental vibrational bands. Table S. 4 shows the IR and Raman wavenumbers, the scaled vibrational wavenumbers and the fundamental modes together with PED %. Table S. 5 contains local symmetry coordinates, appoximate mode description, the obtained multi-scale factors and diagonal force constants by normal coordinate analysis. Fig. 4 illustrate the comparison of both FT-IR and Raman spectra based on experimental and theoretical methods. With multi-scaled normal coordinate analysis, the RMS deviation between experimental and theoretical wavenumbers is obtained as 11.8 cm^{-1}.

3.4.1. Aromatic CH and C=C vibrations

CH vibrations are observed in the range of 3100–3000 cm^{-1} for aromatic compounds. For Raman spectra, these vibrations are strong in the region of 3070–3030 cm^{-1} but skeletal vibrations are not strong [61]. These CH streching vibrations for the title molecule were detected in 3090(m) cm^{-1}, 3075 (m) cm^{-1}, 3068 (sh) cm^{-1} in IR spectrum and 3089 (m) cm^{-1}, 3073(m) cm^{-1}, 3060 (sh) in Raman spectrum. The corresponding wavenumbers were calculated as 3088 cm^{-1}, 3079 cm^{-1}, 3067 cm^{-1} to the monosubsititited benzene ring (ring 3). Aromatic ring C=C stretching vibrations occur in the 1625–1430 region [61,62]. In this study, C=C stretching vibrations were assigned at 1600 (1600), 1594 (1589), 1578 (1575), 1571 cm^{-1} in the Raman spectrum (FT-IR spectrum). The Raman bands here were observed more intensity than in IR. The C=C stretching vibrations out of this region (1345–1494 cm^{-1}) couple with coupled with the in-plane C-H bending vibrations, which are dominant regard of PED.

3.4.2. In-plane CH bending vibrations

In-plane C-H bending vibrations occur between 1300 and 1000 cm^{-1}. However, these bands are not very useful due to the strong absorptions resulted in this region of the spectrum [63]. In the Raman spectrum, in-plane C-H bending vibrations occur in the range 1290–990 and these bands are very strong. In the title molecule, the in-plane C-H bending vibrations of the ortho-di-subsitituted benzene ring were observed in the IR spectrum as 1020 w, 1125 w, 1156 w, 1268 vw, 1480 w in cm^{-1}. These bending vibrations coincide with the C-C streching vibrations of the ring. In theoretical calculations, the frequencies of these bands were calculated as 1010, 1133, 1155, 1281, 1453 cm^{-1}, respectively. On the other hand, in the Raman spectrum of the C-H bends of the molecule, 1160 (m) and 1275 (w) cm^{-1} were observed. The C-H bending vibrations of the mono-subsititue ring of the molecule were observed at 1063 (vw), 1178 (*vs*), 1407 (vw), 1450 (m), 1494 (m) cm^{-1} in the IR spectrum. The reason for the high frequency of these bending vibrations is that they vibrate together with the C-C bonds of the mono-subsitituted benzene ring as in the ortho-di-subsitituted benzene ring. These bending modes were calculated at wavenumbers 1067, 1159, 1443, 1449, 1479 in cm^{-1}, respectively. In addition, C-H bending modes of the mono-subsitituted benzene ring were asssigned at 1407 (w) and 1487 (m) cm^{-1} in the Raman spectrum.

3.4.3. Out-of-plane C-H bendig vibrations

Out-of-plane C-H bending vibrations are observed in the range 900–690 cm^{-1}. The bands of out-of-plane bending vibrations of aromatic compounds are intense and provide information about the hydrogen number in the ring [64]. Out-of-plane bending vibrations are more useful than in-plane bending vibrations [63]. The title has mono-subsitituted and ortho-di-subsitituted benzene structures. Mono-subsitituted rings have two strong absorption bands, one of which occurs between 820–720 cm^{-1} and the other between 710–670 cm^{-1}. The second band is generally less intensity than the first band. The bending vibrations of the mono-subsitituted ring of the title molecule were observed at 756 (w) and 694 (s) cm^{-1}. The frequencies and intensities of these bands are consistent with the literature [63]. Other out-of-plane bending vibrations of the mono-subsitituted ring were assigned at frequencies 848, 896, 957 cm^{-1}. The frequencies of these modes were calculated at wavenumbers 689, 753, 861, 891, 973 cm^{-1}. In addition, out-of-plane bending modes of the mono-subsitituted ring were determined at 690 (vw), 755 (vw), 841 (w), 888 (m) cm^{-1} in the Raman spectrum.

Ortho-di-subsitituted rings show a strong absorption band between 790–720 cm^{-1} [63]. The IR peak at 769 (m) cm^{-1} was attributed to the out of CH bending mode in the ortho-di-subsitituted ring of the title molecule. The other out of plane bending vibration band of the ortho-di-subsitituted ring was observed as a weak band at 979 cm^{-1}. The out of plane bending frequencies of this ring were calculated at 779, 974 cm^{-1}. In addition, a weak band at 923 cm^{-1} observed in the Raman spectrum was assingned to this mode in this ring.

3.4.4. C-N, C-S and S-N Streching vibrations

The C-N vibration was observed to exhibit a very intense band at a wavenumber of 1218 cm^{-1} in the IR spectrum and a moderate band at a wavenumber of 1214 cm^{-1} in the Raman spectrum. This vibrational band was theoretically calculated as 1205 cm^{-1}. In the 2-(4-bromophenyl)-1H-benzimidazole molecule [65], this vibrational mode was observed at 1396 cm^{-1} and 1225 cm^{-1}. The reason for the decrease in the frequency of the C-N vibration may be due to the electronegativitiy (or electronic vicinity) of the N atom, which attracts charge from other atomic groups and accordingly increases the bond length. In the Raman spectrum, coupling of out-of-plane C-N bending and in-plane C-N bending was observed at a wavenumber of 60 cm^{-1}. This band was theoretically calculated at 69 cm^{-1} wavenumber and out-of-plane C-N bending band was observed at 80 cm^{-1} wavenumber. Other in-plane C-N bends were assigned at wavenumbers of 273 cm^{-1}, 347 cm^{-1}, 455 cm^{-1}, 533 cm^{-1}, 896 cm^{-1} respectively.

In the Raman spectrum of the N-phenyl-o-benzene disulfonimide molecule, a very strong band at a wavenumber of 116 cm^{-1} was observed. This band theoretically corresponds to the vibrational mode called butterfly mode vibration. This vibrational mode was observed in the 2-(4-Bromophenyl)-1H-benzimidazolemolecule [65] at a wavenumber of 126 cm^{-1}. The S-N stretching vibration is observed as a band of moderate intensity at 950–860 cm^{-1} [61]. The S-N streching vibration was observed in the experimental spectrum as a moderate intensity peak at 896 cm^{-1} and 946 cm^{-1}, respectively, and these vibrational modes were calculated at wavenumbers 891 cm^{-1} and 939 cm^{-1}. In methyl pseudo saccharyl ether molecule [52], this vibrational mode was observed as a moderate peak at wavenumbers 917 cm^{-1} and 906 cm^{-1}. The reason for the decrease of the S-N stretching vibration to 896 cm^{-1} may be due to the charge flow from the sulfonyl group to this bond. In addition, a decrease in frequency may have occurred due to the vibration of another bond in the molecule at the same frequency. In the Raman spectrum, the stretching vibrations of the S-N bond were observed as moderately strong bands at a wavenumber of 888 cm^{-1} and very weak bands at a wavenumber of 945 cm^{-1}. C-S stretching vibration was observed in the Raman spectrum as weak bands at 339 cm^{-1} and 205 cm^{-1}. It was also observed at wavenumber 730 cm^{-1} in this IR spectrum. In theoretical calculations, these bands were calculated at wavenumbers 327 cm^{-1}, 212 cm^{-1} and 719 cm^{-1}, respectively. The frequencies of this bond are variable in the literature. The reason for the low frequency of this mode in the ttle molecule may be due to electronic interactions or it may be due to cupling with sulfonyl bending modes.

3.4.5. *Sulfonyl* $(SO)_2$ *vibrations*

In the solid phase, sulfonimides exhibit a very intense and broad band in the range 1360–1315 cm^{-1} due to $(SO)_2$ asymmetric stretching vibrations [61]. In this study, $(SO)_2$ asymmetric stretching vibration was observed as a very strong and broad band at a wavenumber of 1345 cm^{-1} and a weak band at a wavenumber of 1325 cm^{-1}. In addition to these bands, a very weak band at 1345 cm^{-1} was observed in the Raman spectrum. These bands were theoretically calculated at 1345 cm^{-1} and 1334 cm^{-1}. In 2-nitrobenzenesulfonamide molecule [65], asymmetric sulfonyl vibrations were determined at 1345 cm^{-1} and 1332 cm^{-1}, and these vibrations were in agreement with them. In the solid phase, sulfonimides exhibit a very strong band in the range of 1180–1140 cm^{-1} due to the symmetrical stretching vibrations of $(SO)_2$ groups [61]. In the title molecule, $(SO)_2$ symmetric stretching vibrations in the experimental IR spectrum, 1180 cm^{-1} (*vs*), 1146 cm^{-1} (s), 1113 cm^{-1} (w) were observed, respectively. In the Raman spectrum, 1178 cm^{-1} (m), 1153 cm^{-1} (w), 1108 cm^{-1} (vw) were observed. Theoretically, these bands were calculated at wavenumbers of 1169 cm^{-1}, 1154 cm^{-1}, 1113 cm^{-1}, respectively. These stretching vibrations of the $(SO)_2$ group are in agreement with the $(SO)_2$ vibrations of the silver-metal complex of saccharin [66]. $(SO)_2$ wagging vibration is observed in the range of 560–480 cm^{-1} [61]. In the title molecule, this bending vibration mode was in the Raman spectrum at a wavenumber of 500 cm^{-1} with a high PED weight (28 %). In addition, the vibrations at 552 cm^{-1}, 562 cm^{-1}, 730 cm^{-1} were observed as coupling with other modes. $(SO)_2$ scissoring bendig vibrations were observed at 620 cm^{-1} in the experimental IR and Raman spectrum with a predominant PED weight. In addition, the vibrations occurring at 552 cm^{-1}, 562 cm^{-1} were coupled. The rocking bending mode of $(SO)_2$ was observed predominantly in the experimental Raman spectrum at a wavenumber of 318 cm^{-1}. This band was theoretically calculated at a wavenumber of 315 $(SO)_2$. The $(SO)_2$ twisting bending mode was observed in the experimental Raman spectrum as a very strong band at a wavenumber of 167 cm^{-1}. This bending mode was theoretically calculated as 188 cm^{-1}.

3.5. *Analysis of UV–visible spectra*

The TD-SCF (B3LYP/6–311++G(d,p)) method with the CPCM solvent medium (DMSO and chloroform) was used to perform a theoretical evaluation of the vertical singlet electronic transitions of the molecule at room temperature (293.15 K). The experimental UV–Vis spectra were presented in Figs. 5(a) and (b) for both solvents. Furthermore, the model chemistry enabled the identification of the oscillator strengths, absorption wavelengths and HOMO-LUMO as the fundamental contributors (>5 %) to the electronic excitations of the title molecule. For the solvents DMSO and chloroform, Tables S. 6 and S. 7 show the related calculated values of the molecule, including the observed absorption wavelengths and the fragment description in the Lewis structure of the UV-visible electronic transitions. In this respect, the Canonical Molecular Orbital (CMO) module implemented in the Natural Bond Orbital (NBO) program NBO 7.0 is used to find the NBO composition of each canonical molecular orbital (occupied and virtual) as well as both the bonding and antibonding percentages, generating the Lewis description of the UV electronic transitions in the title molecule. The oscillator strengths of zero were identified as forbidden transitions and no band was assigned for them. In addition, high oscillator strength values from the calculation for intense absorption bands were selected for assignment.

In the DMSO environment (Ɛ=46.826) in Table S . 6, the electronic excitation and absorption bands were theoretically found at wavelengths of 252.05, 250.77, 242.33, 241.77, 237.48, 232.64, 231.21, 223.86, 219.65, 219.07, 217.63, 214.21 nm. The corresponding oscillator strengths (energy gaps eV) were also estimated to be 0.0112 (4.9191), 0.0338 (4.9441), 0.0356 (5.1163), 0.0000 (5. 1283), 0.0418 (5.2208), 0.0000 (5.3295), 0.0000 (5.3624), 0.1027 (5.5384), 0.5055 (5.6447), 0.0095 (5.6596), 0.2771 (5.6969), 0.0007 (5.7881). The excitation band at 286 nm was assigned to $\pi \rightarrow \pi^*$ from the phenyl ring (ring 3) to the fused ring (ring 1). The resulting band assignments are not pure $\pi \rightarrow \pi^*$ transitions. The $n \rightarrow \pi^*$ transitions usually contribute to the $\pi \rightarrow \pi^*$ transitions. As can be seen in Table S. 6, the absorption bands at 263 and 276 nm are predominantly the $\pi \rightarrow \pi^*$ transitions.

In the chloroform phase (Ɛ=4.7113) in Table S. 7, the electronic excitation and absorption bands at wavelengths 255.80, 254.48, 246.42, 242.49, 237.39, 237.32, 235.82, 224.37, 224.22, 219.95, 217.12 and 212. 72 nm with oscillator strengths (related energy gaps eV) of 0.0052 (4.8469), 0.0243 (4.8720), 0.0008 (5.0314), 0.0223 (5.1130), 0.0307 (5. 2229), 0.0000 (5.2244), 0.0001 (5.2576), 0.0904 (5.5260), 0.0763 (5.5260), 0.0098 (5.6369), 0.5190 (5.7103) and 0.0004 (5.8285), respectively. Mono-substituted benzene derivatives absorb UV-visible light in the range 200–280 nm. The first band appears at 250–280 nm and the second band appears at 200–250 nm [67]. The absorption band

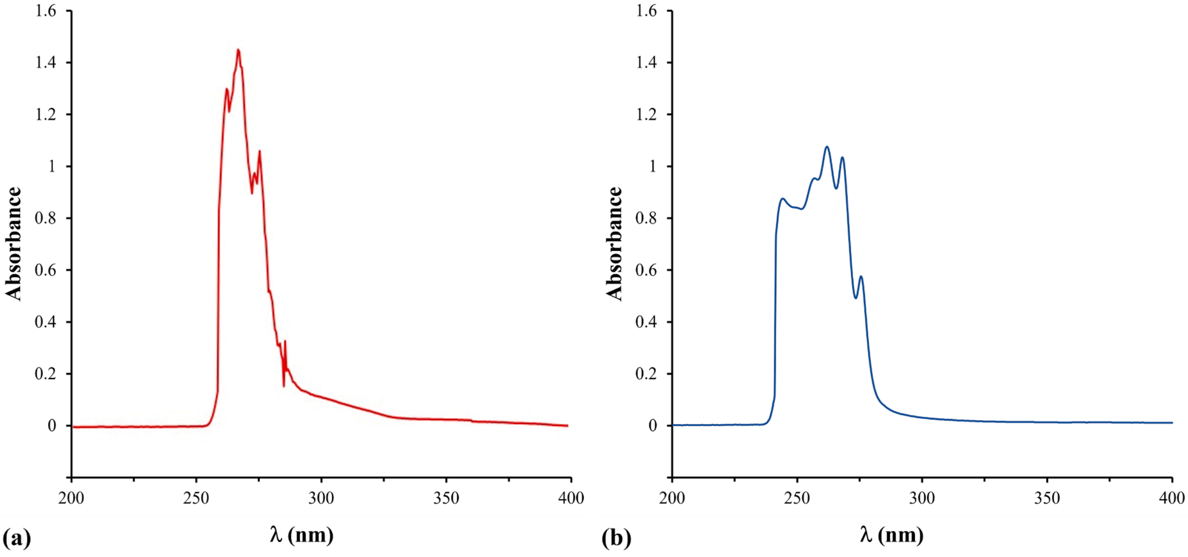

Fig. 5. UV-vis spectra of the title molecule measured in (a) DMSO and (b) chloroform medium.

of 275 nm was assigned to the pure π →π* transition between ring 3 and ring 1. The observed band at 268 nm is predominantly its own π →π* transition of the fused ring, as in addition to the n→π* transitions in the vicinity. The excitation band at 262 nm is the π →π* transition in ring 3, while the absorption band at 249 nm is the π →π* transition in ring 1 with the n→π* contribution.

The solvent environment has a degree of influence on the transition band character of compounds [68]. In the solvent environment of increased polarity from chloroform to DMSO, the π →π* transition of the title molecule shifts to a longer wavelength from 275 to 286 nm (the first transition in Tables S. 6 and S. 7), known as the red shift. Similarly, the π →π* absorption band of 268 nm in the chloroform solvent undergoes a shift to 276 nm in the DMSO solvent by moving up the accompanying n →π* bands, but the percentage probability of the HOMO-LUMO transition changes due to the solvent polarity. Other observed bands show such similarities.

3.6. Analysis of NMR spectra

NMR is a significant spectroscopic technique that can be employed to ascertain the number of magnetically distinct atoms present within any given molecule. Even though many nuclei are studied by NMR techniques, ^{1}H- and ^{13}CNMR are the most commonly used. The combination of the NMR spectrum and chemical shift calculations provides an invaluable tool for elucidating molecular structure. Although DFT methods are less accurate than post HF methods, they are nevertheless capable of estimating the theoretical values of the ^{13}C- and ^{1}HNMR chemical shifts with a high degree of accuracy in comparison to the available experimental data. In this study, the ^{13}C- and ^{1}HNMR chemical shifts of the title molecule were calculated at the base set levels 6–311++G(d,p), cc-pV5Z, aug-cc-pV5Z, and DGDZVP of B3LYP theory, as well as at the theory level PBEPBE/DGDZVP. These ^{13}C- and ^{1}HNMR chemical shifts are presented in Tables S. 8 and S. 9 in comparison with the related experimental values, respectively, together with the TMS value for each model chemistry. Additionally, experimental ^{1}H- and ^{13}CNMR spectra of the title molecule were given in Figs. S1 and S2. Our molecule has two conformers, S_1 and S_2. Since the NMR chemical shifts are the result of a dynamic process, they are averaged over the Boltzmann canonical distribution in a dynamic equilibrium [69]. However, we used the S_1 conformer for the chemical shift calculation because S_1 and S_2 have the same standard Gibbs free energy.

Chemical shifts for aromatic ring carbons generally occur in the range 110–175 ppm. Here, fused ring carbons (ring 1) have chemical shifts in the range 124–137 ppm. C_1 and C_2 have the same chemical environment, called equivalent carbons, as in C_3 and C_6, in C_4 and C_4. Optimization shows that they are the same plane symmetry. However, the chemical shift of C_4 and C_5 (*ca.* 137 ppm) appears at a lower field value than that of C_3 and C_6 (*ca.* 124 ppm) as well as C_1 and C_2 (*ca.* 132 ppm). As the C_4 and C_5 carbon atoms are lower electronegativity than sulphur atoms they link to, they shift to lower field, and also produce a high chemical shift. On the other hand, the ^{13}C chemical shifts for the phenyl ring (ring 3) are detected in the range of 125–134 ppm. C_{16} and C_{18} are chemical equivalents because of the same chemical shifts (131.34 ppm), but not the others because the plane symmetry breaks down due steric effect. For the C_{14} carbon atom, a significantly low chemical shift was observed at *ca.* 125 ppm due to the high charge density.

Chemical shifts of hydrogens attached to an aromatic ring are in the range of 6.5–8.0 ppm. In ring1 (fused ring) ^{1}H chemical shifts of 8.22 ppm were observed for H_{20} and H_{21} and 8.60 ppm for H_{22} and H_{23}. The reason for this is a different hybridisation of the carbons to which the hydrogens are attached. While the C_1 (or C_2) atom to which the H_{20} (or H_{21}) atom is bonded has a hybridisation of $sp^{2.6}$, the C_3 (or C_6) atom to which the H_{22} (or H_{23}) atom is bonded has a hybridisation of $sp^{2.52}$. Here, the $sp^{2.52}$ carbon atoms become more less shielding for the H_{22} and atoms. For ring 3 (phenyl ring), the H_{24} and H_{26} (H_{25} and H_{27}) have the same chemical environment, and their chemical shifts are detected at 7.61 ppm (7.74).

Finally, we have considered the effect of the base set on the chemical shifts for the DFT (B3LYP). For the ^{13}C chemical shifts some statistical results have been presented in Table S. 8. Here, the formulae of the statistical definition are given in the supplementary data section. Among the base sets combined with B3LYP, the best MAPE result was obtained with an error of 4.69 % for B3LYP/cc-pVZT. On the other hand, the MAE values for B3LYP/DGDZVP and PBEPBE/DGTZVP were calculated to be 5.78 % and 6.98 %, respectively. Although the base set of DGTZVP (triple zeta valence set) is larger than that of DGDZVP (double zeta valence set), in combination with PBEPBE it results in a small deviation in the chemical shift calculation of carbon atoms. Regarding the base set effect on the ^{1}H chemical shift calculations in Table S. 9, the best MAPE value was again found for B3lyp/cc-pVZT with an error of 3.47 %. The B3LYP/6–311++G(d,p) (3.68 %) and B3LYP/DGDZVP (3.68 %) methods produce similar results for the ^{1}H chemical shift calculations. In addition, the linear fit plots between experimental and theoretical chemical shifts for each quantum chemical model are included in Fig. 6.

3.7. Druggability analysis

Using SwissTargetPrediction, we identified CA metalloenzymes as the most likely targets of the title molecule . To validate this prediction, we applied the same methodology to VD10–50, a known experimental inhibitor of CA [70]. The results showed that the title molecule had the same overall probability of targeting CA enzymes as VD10–50 (33.3 %) (Fig. 7). However, the title molecule was more likely than VD10–50 to specifically target CA II and CA XII enzymes (22 % *vs.* 12 %; Table 5). This suggests that the title molecule not only has the potential to target these enzymes but may also exhibit stronger or more selective affinity against them.

Following target identification, we performed molecular docking calculations to assess the binding affinity and potential binding modes of the title molecule and VD10–50 inhibitor with CA II and CA XII enzymes. The inhibitory activity of the title molecule and the VD10–50 inhibitor were examined against both isoforms to assess their selective inhibition activity. Figs. 8 (a) and (b) show the docking positions where the title molecule binds most efficiently with the active sites of CA II and CA XII. For comparison, we also included the docking poses of the experimental inhibitor in this figure. As shown, the docked ligand occupies the same binding pocket as the experimental inhibitors in both enzyme-ligand complexes. This positional alignment provides evidence that the title molecule may exhibit inhibitory activity against these CA enzymes. Furthermore, the 2D diagrams of enzyme-ligand interactions in this figure indicate that the title molecule forms similar interactions to the VD10–50 inhibitor with key active site residues of the CA enzymes, including hydrogen bonds, π-cation interactions, and π-π stacking. Notably, the title molecule also forms a covalent bond with the Zn(II) ion in the active site, just like the experimental inhibitor, which further strengthens its potential inhibitory activity.

To further evaluate the inhibitory activity, we performed docking calculations to estimate the binding energies and Ki values for both the title molecule and VD10–50. The results are summarized in Table 6. The -title molecule demonstrates promising inhibitory activity against both enzymes, with Ki values in the μM range, comparable to the experimental inhibitor. Notably, a comparison of these values shows that the Ki of the title molecule against CA XII is approximately seven times lower than that of the VD10–50 inhibitor, suggesting that the title molecule may be more effective than the experimental inhibitor. Furthermore, the data indicate selective inhibition of the CA XII isoform, as the Ki value for CA XII is about six times lower than for CA II. This selective inhibition is a crucial aspect, as previously mentioned, because targeting CA XII holds significant potential for developing novel cancer therapies.

The correlation between local reactivity descriptors and enzyme-

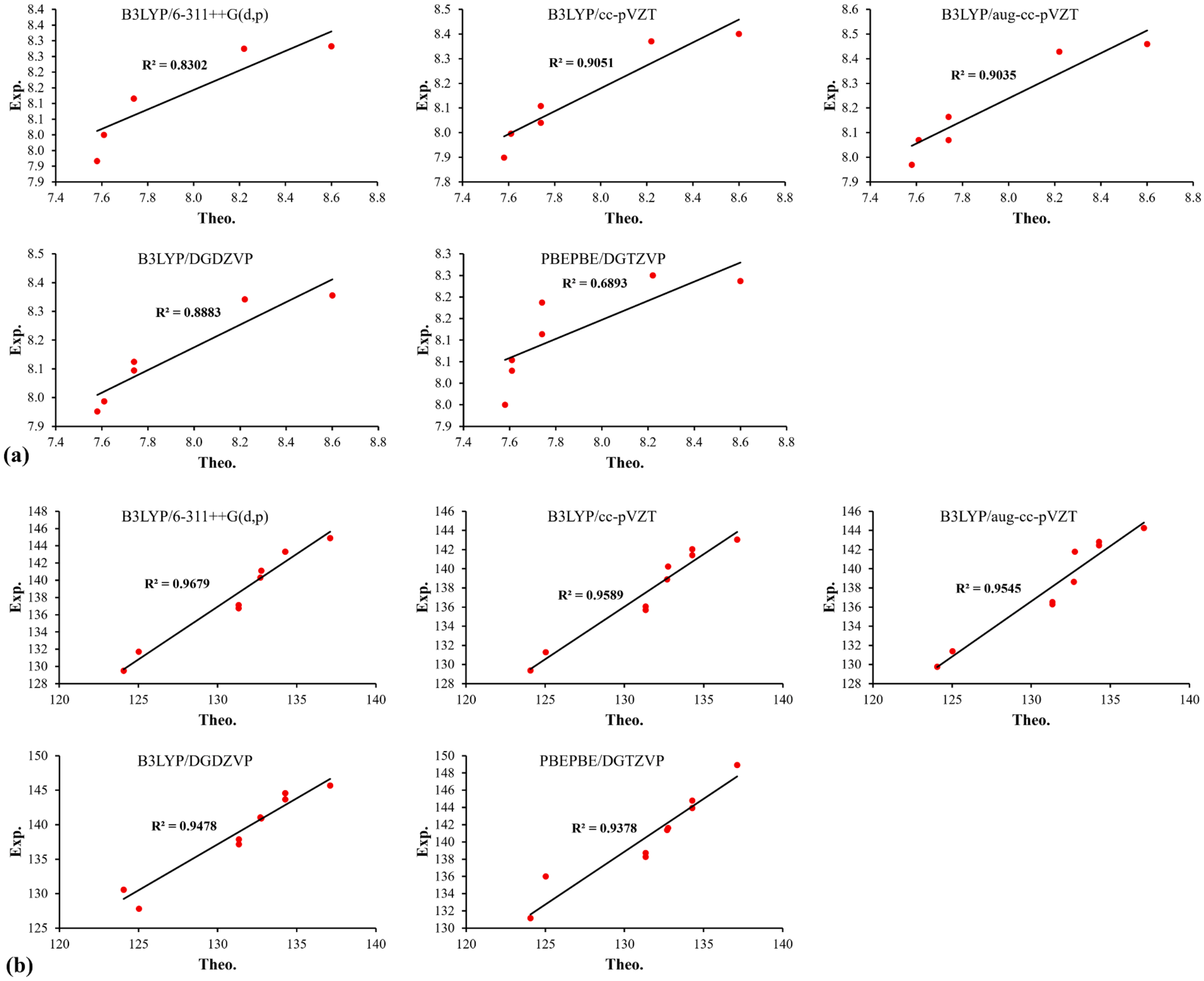

Fig. 6. Linear fit plots of (a) ^{1}H- and (b) ^{13}CNMR chemical shift (ppm) in DMSO.

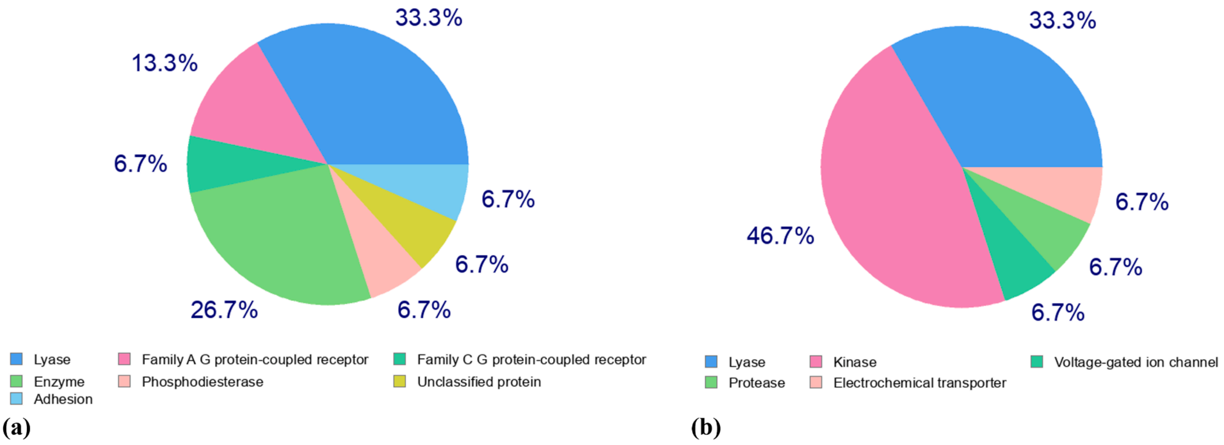

Fig. 7. Target class distribution of (a) the title molecule and (b) VD10–50 based on SwissTargetPrediction analysis. The pie charts represent the percentage of predicted target classes for each compound.

ligand interactions provides valuable insights into how the electronic properties of the ligand influence its binding affinity and specificity toward the enzyme's active site. In enzyme-ligand interactions, the electrophilic regions of the enzyme preferentially interact with the nucleophilic regions of the ligand, facilitating binding and stabilization [71]. By considering the partial charges presented in Table S2, the molecular electrostatic potential (MEP) of the title molecule can be compared with its inhibitory activity against CA enzymes. The sulfur atoms, which carry a partial charge of +0.691e, are the primary sites of positive charge, as revealed by NBO analysis. With a bond order of 3.77 and the potential to form up to four bonds, these sulfur atoms may engage in π-cation interactions with histidine residues of the CA enzymes (Fig. 8). An electrostatic interaction between the Zn(II) ion at the active site and the oxygen atom of the ligand, located in the

Table 5
SwissTargetPrediction web service prediction of the possible targets of our compound and VD10–50, which has been tested as a sulfonamide inhibitor for CA.

	Target	Target Class	Probability
Title molecule	Carbonic anhydrase XII	Lyase	22.2
	Carbonic anhydrase II	Lyase	22.2
	Carbonic anhydrase IX	Lyase	22.2
	Carbonic anhydrase I	Lyase	13.6
	Carbonic anhydrase XIII (by homology)	Lyase	11.2
	Serotonin 6 (5-HT6) receptor	Family A G protein-coupled receptor	11.2
	Metabotropic glutamate receptor 4	Family C G protein-coupled receptor	0.0
	Aldehyde reductase (by homology)	Enzyme	0.0
VD10–50	Carbonic anhydrase XII	Lyase	12.0
	Carbonic anhydrase II	Lyase	12.0
	Carbonic anhydrase I	Lyase	12.0
	Carbonic anhydrase VII	Lyase	11.2
	Carbonic anhydrase XIII	Lyase	11.2
	MAP kinase-activated protein kinase 2	Kinase	11.2
	Ephrin receptor	Kinase	11.2
	Epidermal growth factor receptor erbB1	Kinase	11.2

high-electron-density red region of the MEP map (Fig. 3), is anticipated. This interaction likely results in the formation of a covalent bond, as illustrated in Fig. 8. Additionally, the oxygen atoms in the red region exhibit potential to form hydrogen bonds with X-H groups, particularly those in Thr residues (Fig. 3 and Fig. 8). NBO and MEP analyses further highlight that the phenyl rings of the title molecule, as sources of delocalized π clouds, enable π-π and π-alkyl interactions, contributing to the ligand's effective binding with the CA enzymes.

Furthermore, the energy gap between the HOMO and LUMO significantly influences the chemical and biological behavior of the molecule, as it determines the molecule's reactivity and interaction with biological targets [62,72]. As illustrated in Fig. 8, the HOMO of the ligand's phenyl ring region may participate in weak π-alkyl interactions with the CA enzymes, contributing to ligand stabilization at the binding site. Although such interactions are generally weaker, they may support the ligand's overall binding affinity. FMO analysis indicates that the -SO_2-N-SO_2 fragment contributes minimally to electrophilic interactions but suggests that the sulfur atoms within this fragment are favorable sites for π-cation interactions with the enzymes. These sulfur atoms are well-suited for engaging in stabilizing interactions with the positively charged residues near the active site of CA enzymes. Furthermore, the oxygen atoms in the -SO_2-N-SO_2 fragment exhibit potential to form hydrogen bonds through nucleophilic attack with the X-H groups of enzymes, such as those in the Thr residues. Notably, the oxygen atom O_{12}, with a dual descriptor value less than zero, is identified as an electrophilic attack site. This suggests its ability to interact covalently with the Zn(II) ion in the active site of CA enzymes, further stabilizing the enzyme-ligand complex. These interactions collectively highlight the role of electronic properties in defining the ligand's binding mechanisms and specificity toward CA enzymes.

To validate the stability and binding dynamics of the title molecule and the VD10–50 inhibitor within the active sites of CA II and CA XII, we performed molecular dynamics (MD) simulations for both compounds. In Fig. 9, the distance between the Zn atom in the enzyme's active site and the O atom of the ligand molecules is quantified to demonstrate the stability of the enzyme-ligand complexes during the 100 ns MD simulations. In Fig. 9 (a), the CA II- title molecule complex (gray line) shows a significant increase in distance after approximately 20 ns, indicating that the title molecule has moved away from the Zn atom and left the active site. This suggests instability in the CA II-title molecule complex, as the ligand did not maintain close contact with the active site. In contrast, the other three complexes, CA XII- title molecule (red line), CA II-VD10–50 (green line), and CA XII-VD10–50 (blue line), display consistent distances that remain close to the Zn atom during the simulation, indicating stable binding. This stability suggests that the ligands remain within the active site of the enzyme, particularly for CA XII, where both ligands (the title molecule and VD10–50) stay bound. Fig. 9 (b) provides structural snapshots and a bar plot showing the average distance for each complex over the final 20 ns. The snapshots clearly depict that in the CA II-title molecule complex, the title molecule has moved farther from the Zn atom, while in the CA XII-title molecule, CA II- VD10–50, and CA XII- VD10–50 complexes, the ligands remain close to the Zn atom. The bar plot also reflects this finding, showing a higher average distance for the CA II-title molecule complex compared to the other complexes. These results suggest selective inhibition of CA XII by the title molecule, as it remains bound within the active site of CA XII but not in CA II. Conversely, the VD10–50 ligand demonstrates stable binding with both CA II and CA XII, suggesting it can inhibit both enzymes. This backs up the idea that the title molecule can only block CA XII, while the experimental ligand (VD10–50) blocks both CA II and CA XII. It seems that this selective inhibition by the title molecule may be attributed to differences in the active sites of CA II and CA XII, which differ by several residues. These differences in the active site likely influence the binding stability of the title molecule, allowing it to inhibit CA XII more effectively while destabilizing its interaction with CA II.

Finally, we performed ADMET analysis on the title molecule to evaluate its pharmacokinetic properties, safety profile, and overall drug-likeness. The key findings from this analysis are summarized in Table 7. It shows that the title molecule demonstrates moderate absorption and bioavailability, indicating that while it has the potential to be orally available, further optimization may be needed to enhance its systemic exposure. The ligand shows moderate lipophilicity, which provides a good balance for membrane permeability, though solubility issues may still need to be addressed for optimal absorption. In terms of BBB penetration, the title molecule shows moderate potential, suggesting it could have some CNS effects but is not highly suited for CNS-targeted therapies. A major limitation is its very high PPB (98.6 %), which significantly reduces the amount of free drug available in circulation, potentially limiting its pharmacological activity. On the positive side, the title molecule exhibits very low potential for CYP3A4 inhibition, minimizing the risk of drug-drug interactions and ensuring stable metabolism. This makes it a safer candidate in terms of metabolic interactions. However, the ligand's high risk of hepatotoxicity is a major concern, requiring careful monitoring or optimization to reduce the likelihood of liver damage. The ligand has moderate renal clearance, meaning it will likely be excreted at a reasonable rate, balancing its potential half-life and dosing frequency. Additionally, it shows a low risk of hERG inhibition, minimizing the potential for cardiotoxicity. Overall, despite the favorable metabolic and safety properties of the title molecule, such as its low CYP3A4 inhibition and low hERG risk, its high PPB and hepatotoxicity risk should be addresed to enhance its draggability and therapeutic potential.

4. Conclusion

In this study, N-phenyl-o-benzenedisulfonimide, a disulfonimide, was investigated through spectroscopic analyses and DFT calculations to provide a detailed characterization of its properties. Specifically, X-ray crystallography, FT-IR, FT-Raman, UV-vis, and NMR spectroscopy were employed to elucidate both the molecular structure and spectroscopic behavior of the compound. The NoSpherA2 method was employed to accurately determine the positions of the hydrogen atoms within the crystal structure, revealing four intermolecular C-H···O hydrogen bonds. Vibrational analysis, based on normal coordinate treatment, was conducted using multi-scaling between the experimental and harmonic force constant matrices at the B3LYP/6–31G(d) level of theory. A good

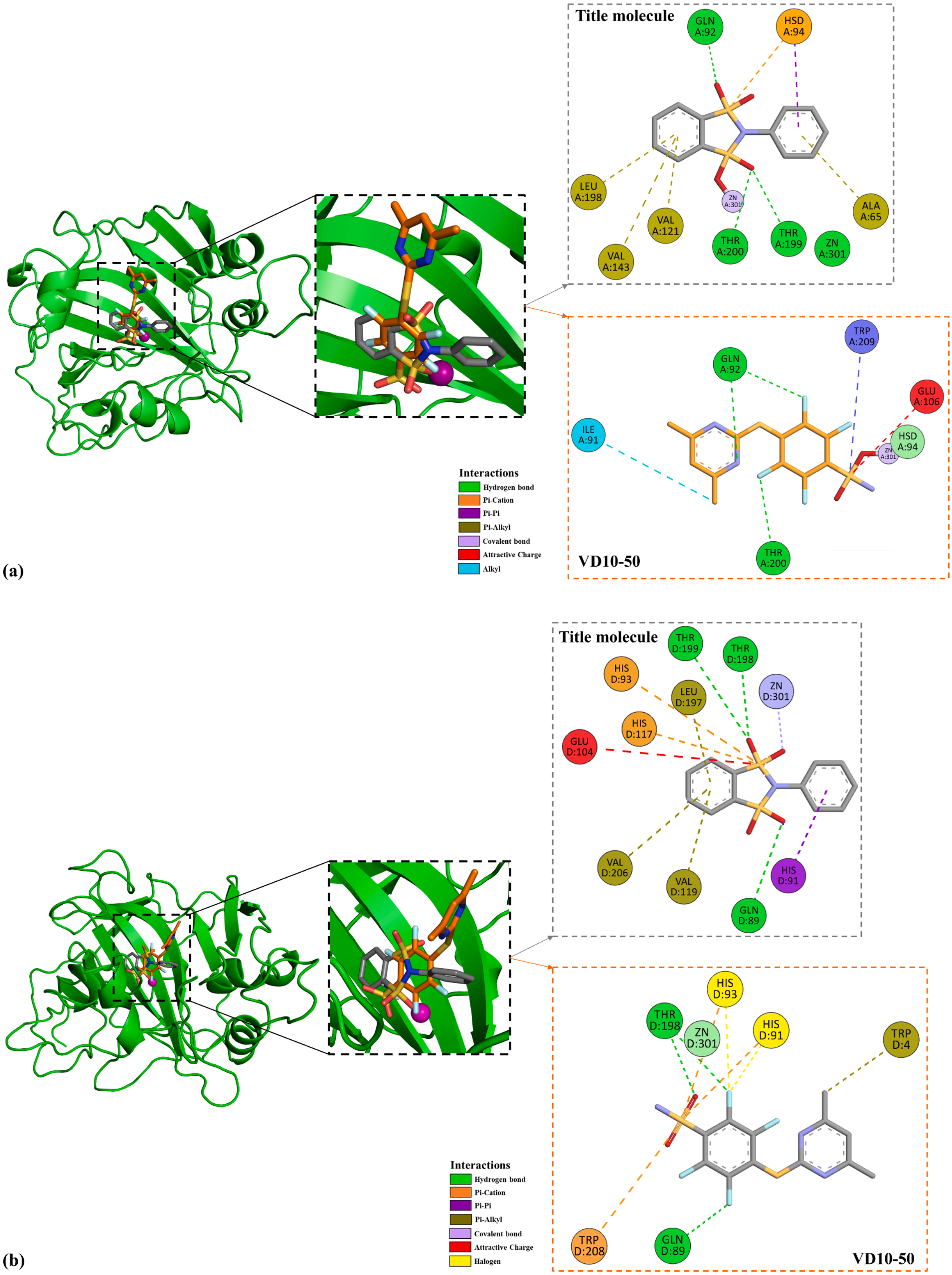

Fig. 8. The best docked poses of the title compound into the active sites of the (a) CA II (PDB ID 4ht0 [51] and (b) CA XII (PDB ID 6yhb [52]) enzymes, accompanied by a comparative analysis of VD10–50 inhibitor. The -title compound is depicted as gray sticks, the experimental inhibitor as orange sticks, and the backbone of the enzyme as a green cartoon. Additionally, a 2D diagram and the binding mode of the enzyme-ligand interactions in the active sites are shown.

Table 6
Predicted binding energies and Ki values for Carbonic anhydrase (CA)-ligand complexes from docking calculations.

Compound	Predicted binding energy (kcal/mol)		Estimated K_i (μM)	
	CA II	CA XII	CA II	CA XII
VD10–50[*]	-8.68 ±0.03	-7.73 ±0.06	0.43	2.15
Title molecule	-7.83 ±0.11	-8.84 ±0.12	1.82	0.32

[*] A tested CA inhibitor taken from the reference [70].

fit between the experimental and theoretical force constants was achieved, with an RMS value of 11.8 cm^{-1}, and the scale factors obtained can be applied to the vibrational analysis of similar molecules. Furthermore, both symmetric and asymmetric stretching vibrations of the sulfonyl groups were identified using FT-IR and FT-Raman spectroscopies and were found to occur within the range of 1108–1345 cm^{-1}.

In addition, conformational analysis revealed two stable conformers of the compound, with conformer S_1 being the most stable. A comparison of the optimized DFT geometrical parameters with crystallographic data showed suitable agreement between them for conformer S_1. For this conformer, the ^{1}H- and ^{13}CNMR chemical shifts were calculated at different computational levels and compared with experimental values. A good agreement was found between the calculated at B3LYP/cc-pVZT level of theory and experimental results, confirming that selecting conformer S_1 was appropriate for evaluating the properties of this compound. Furthermore, the calculated UV-vis spectra revealed that the most significant transitions in the compound were $\pi \rightarrow \pi^*$ transitions, occurring on both benzene rings. NBO analysis supported these findings by showing charge transfer energies between the atomic orbitals of the compound, with magnitudes ranging from 10 to 30 kcal/mol.

Finally, we performed a comprehensive druggability analysis of the title molecule, which included target prediction, molecular docking calculations, MD simulations, and ADMET analysis. This detailed computational approach identified the compound's binding potential, stability, and pharmacokinetic properties. Notably, docking and MD simulations revealed the selective inhibition of the CA XII enzyme, a key target in cancer treatment, underscoring its potential as a promising candidate for the development of novel anticancer therapies. Additionally, theoretical insights into local reactivity descriptors, including MEP maps, NBO analysis, and HOMO-LUMO energy gaps, provided a deeper understanding of the enzyme-ligand interactions. These findings underscored the critical role of electronic properties in modulating the compound's inhibitory activity, further supporting its possible therapeutic value.

Table 7
Predicted ADMET properties and DrugBank percentile comparisons for our compound.

Property	**Title molecule**	
	Prediction	Drug Bank Percentile
Absorption		
• Human Intestinal Absorption (HIA)	0.99	47.4
• Oral Bioavailability	0.73	40.5
• Lipophilicity	0.87	40.1
Distribution		
• Blood-Brain Barrier (BBB) Penetration	0.68	44.6
• Plasma Protein Binding (PPB)	98.6	88.8
Metabolism		
• CYP3A4 Inhibition	4.28e-03	26.4
Excretion		
• Renal Clearance (uL/min/mg)	33.70	47.6
Toxicity		
• Hepatotoxicity	0.97	95.9
• hERG Inhibition	0.08	26.6

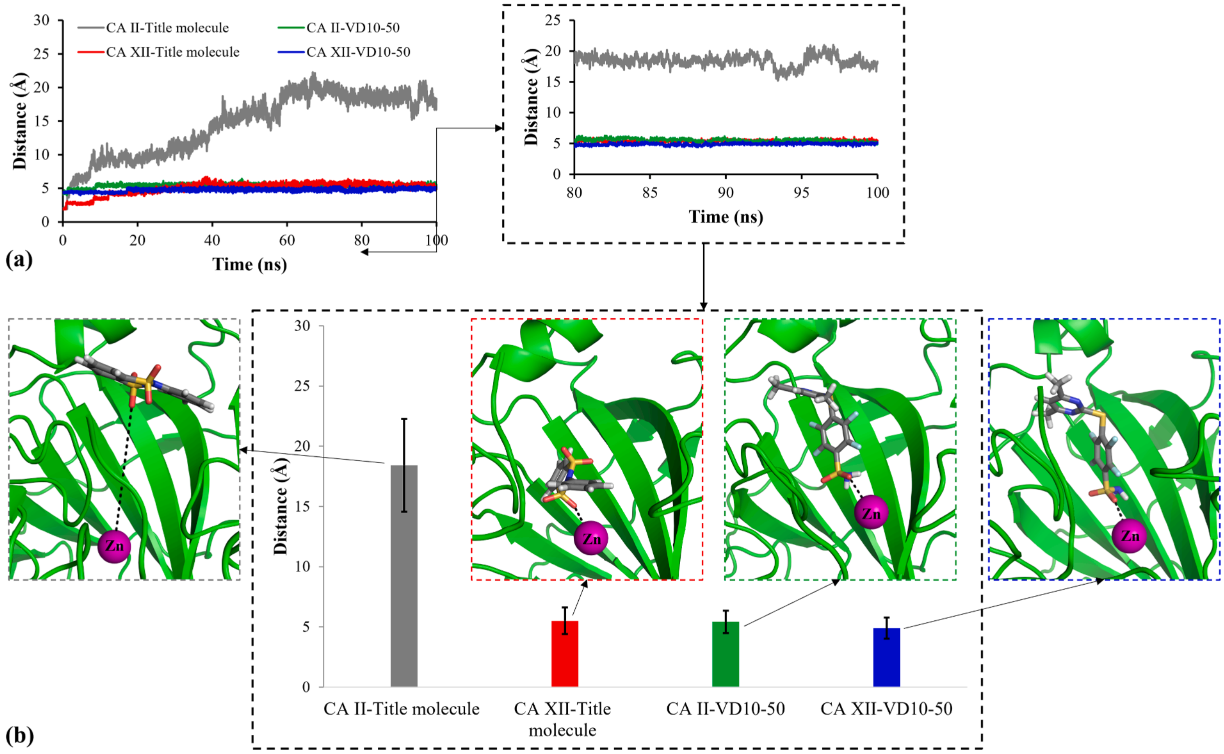

Fig. 9. (a) Time-dependent distance between the Zn atom in the enzyme's active site and the O atom of the ligand in various enzyme-ligand complexes. (b) Structural snapshots and bar plot showing the average distance for each complex during the final 20 ns, with error bars representing the standard deviation derived from three replicates. Enzymes are represented as green cartoons, Zn atoms as magenta spheres, and ligand molecules as color-coded sticks.

CRediT authorship contribution statement

Sedat Gumus: Writing – review & editing, Writing – original draft, Software, Investigation, Conceptualization. **Mohammad Sadegh Sadeghi Googheri:** Writing – review & editing, Resources, Investigation. **Ahmet Gokhan Kazan:** Investigation, Data curation. **Bilge Eren:** Investigation, Data curation.

Declaration of competing interest

The authors declare that they have no known competing financial interests or personal relationships that could have appeared to influence the work reported in this article.

Acknowledgements

The numerical calculations reported in this paper were partially performed at TUBITAK ULAKBIM, High Performance and Grid Computing Center (TRUBA resources). The authors acknowledge Scientific and Technological Research Application and Research Center, Sinop University, Turkey, for the use of the Bruker D8-QUEST diffractometer.

Supplementary materials

Supplementary material associated with this article can be found, in the online version, at doi:10.1016/j.molstruc.2024.141192.

Data availability

Data will be made available on request.

References

[1] M.I. Page, P.S. Hinchliffe, J.M. Wood, L.P. Harding, A.P. Laws, Bioorg. Med. Chem. Lett. 13 (2003) 4489–4492.
[2] S.M. Drawz, R.A. Bonomo, Clin. Microbiol. Rev. 23 (2010) 160–201.
[3] C.T. Supuran, Expert. Opin. Ther. Pat. 28 (2018) 709–712.
[4] C.T. Supuran, A. Scozzafava, Expert. Opin. Ther. Pat. 10 (2000) 575–600.
[5] C.T. Supuran, F. Briganti, S. Tilli, W.R. Chegwidden, A. Scozzafava, Bioorg. Med. Chem. 9 (2001) 703–714.
[6] W.M. Eldehna, M. Fares, M. Ceruso, H.A. Ghabbour, S.M. Abou-Seri, H.A. Abdel-Aziz, et al., Eur. J. Med. Chem. 110 (2016) 259–266.
[7] C.T. Supuran, J. Enzyme Inhib. Med. Chem. 27 (2012) 759–772.
[8] Y. Wan, G. Fang, H. Chen, X. Deng, Z. Tang, Eur. J. Med. Chem. 226 (2021) 113837.
[9] L. Hiepp, D. Mayr, K. Gärtner, E. Schmoeckel, F. Klauschen, A. Burges, et al., PLoS. One 17 (2022) e0271630.
[10] Kopecka, J., Campia, I., Jacobs, A., Frei, A.P., Ghigo, D., Wollscheid, B., et al. Oncotarget. 2015, 6, 6776–93.
[11] G. Li, T.W. Chen, A.C. Nickel, S. Muhammad, H.J. Steiger, T. Tzaridis, et al., Onco Targets. Ther. 14 (2021) 1707–1718.
[12] S. Daunys, V. Petrikaitė, Biol. Cell 112 (2020) 383–397.
[13] M. Kciuk, A. Gielecińska, S. Mujwar, M. Mojzych, B. Marciniak, R. Drozda, et al., J. Enzyme Inhib. Med. Chem. 37 (2022) 1278–1298.
[14] W.M. Eldehna, M.A. El Hassab, N.A. Abdelshafi, R.A. Eissa, N.H. Diab, E. H. Mohamed, et al., Int. J. Pharm. 631 (2023) 122537.
[15] M.Y. Mboge, R. McKenna, S.C. Frost, Top. AntiCancer Res. 5 (2015) 3–42.
[16] K.F. Tonissen, S.A. Poulsen, Cancer Drug Resistance (Alhambra, Calif.). 4 (2021) 343–355.
[17] C.T. Supuran, Met. Based. Drugs 2 (1995) 331–336.
[18] S. Takata, Y. Endo, M. Shahid Ullah, S. Itsuno, RSC. Adv. 6 (2016) 72300–72305.
[19] G. Cheng, Q. Jun, X. Zhang, D. Verdugo, M.L. Larter, R. Christie, et al., Tetrahedron. 53 (1997) 4145–4158.
[20] Y. Bekdemir, B. Eren, H. Kütük, Phosphorus. Sulfur. Silicon. Relat. Elem. 187 (2012) 689–696.
[21] A. Daina, O. Michielin, V. Zoete, Nucleic. Acids. Res. 47 (2019) W357–WW64.
[22] G. Lanka, D. Begum, S. Banerjee, N. Adhikari, Y. P, B Ghosh, Comput. Biol. Med. 166 (2023) 107481.
[23] S. Banerjee, S. Jana, T. Jha, B. Ghosh, N. Adhikari, Comput. Biol. Chem. 110 (2024) 108051.
[24] K. Swanson, P. Walther, J. Leitz, S. Mukherjee, J.C. Wu, R.V. Shivnaraine, et al., Bioinformatics. (2024) 40.
[25] O.V. Dolomanov, L.J. Bourhis, R.J. Gildea, J.A.K. Howard, H. Puschmann, J. Appl. Crystallogr. 42 (2009) 339–341.
[26] L.J. Bourhis, O.V. Dolomanov, R.J. Gildea, J.A. Howard, H. Puschmann, Acta crystallographica. Sect. A, Found. Adv. 71 (2015) 59–75.
[27] G. Sheldrick, Acta Crystallographica Sect. C 71 (2015) 3–8.
[28] L. Midgley, L.J. Bourhis, O.V. Dolomanov, S. Grabowsky, F. Kleemiss, H. Puschmann, et al., Acta Crystallographica Sect. A 77 (2021) 519–533.
[29] F. Kleemiss, P. Puylaert, D. Duvinage, M. Fugel, K. Sugimoto, J. Beckmann, et al., Ibuprofen and sila-ibuprofen: polarization effects in the crystal and enzyme environments, Acta Crystallogr. B Struct. Sci. Cryst. Eng. Mater. 77 (Pt 6) (2021 Nov 12) 892–905, https://doi.org/10.1107/S2052520621009379, eCollection 2021 Dec 1.
[30] F. Neese, WIREs Comput. Mol. Sci. 12 (2022) e1606.
[31] F. Neese, WIREs Comput. Mol. Sci. 2 (2012) 73–78.
[32] Frisch, M.J., Trucks, G.W., Schlegel, H.B., Scuseria, G.E., Robb, M.A., Cheeseman, J.R., et al., Wallingford, CT, 2016.
[33] T. Sundius, J. Mol. Struct. 218 (1990) 321–326.
[34] Sundius, T. Vib. Spectrosc. 2002, 29, 89–95.
[35] D. Michalska, R. Wysokiński, Chem. Phys. Lett. 403 (2005) 211–217.
[36] Istvan, K. Budapest: chemical research center.(It was obtained from Dr. Gabor Keresztury in Chemical Research Center in Budapest). 2002.
[37] E.D. Glendening, J.K. Badenhoop, A.E. Reed, J.E. Carpenter, J.A. Bohmann, C. M. Morales, P. Karafiloglou, C.R. Landis, F. Weinhold, Theoretical Chemistry Institute, University of Wisconsin, Madison, 2018.
[38] J. Sánchez-Márquez, D. Zorrilla, A. Sánchez-Coronilla, D.M. de los Santos, J. Navas, C. Fernández-Lorenzo, et al., J. Mol. Model. 20 (2014) 2492.
[39] G.M. Morris, R. Huey, W. Lindstrom, M.F. Sanner, R.K. Belew, D.S. Goodsell, et al., J. Comput. Chem. 30 (2009) 2785–2791.
[40] J. Eberhardt, D. Santos-Martins, A.F. Tillack, S. Forli, J. Chem. Inf. Model. 61 (2021) 3891–3898.
[41] Guex, N., Peitsch, M.C. Electrophoresis. 1997, 18, 2714–23.
[42] M.J. Abraham, T. Murtola, R. Schulz, S. Páll, J.C. Smith, B. Hess, et al., SoftwareX. 1-2 (2015) 19–25.
[43] V. Hornak, R. Abel, A. Okur, B. Strockbine, A. Roitberg, C. Simmerling, Proteins: Struct., Funct., Bioinf 65 (2006) 712–725.
[44] J. Wang, R.M. Wolf, J.W. Caldwell, P.A. Kollman, D.A. Case, J. Comput. Chem. 25 (2004) 1157–1174.
[45] A.W.S. Da Silva, W.F. Vranken, BMC Res. Notes. 5 (2012) 367.
[46] D.J. Price, III, C.L. Brooks, J. Chem. Phys. 121 (2004) 10096–10103.
[47] G. Bussi, D. Donadio, M. Parrinello, J. Chem. Phys. 126 (2007) 014101.
[48] M. Parrinello, A. Rahman, J. Appl. Phys. 52 (1981) 7182–7190.
[49] T. Darden, D. York, L. Pedersen, J. Chem. Phys. 98 (1993) 10089–10092.
[50] B. Hess, H. Bekker, H.J. Berendsen, J.G. Fraaije, J. Comput. Chem. 18 (1997) 1463–1472.
[51] J.F. Wishart, Radiation and radical chemistry of ionic liquids for energy applications. Ionic Liquids: Current State and Future Directions, American Chemical Society, 2017, pp. 251–272. Vol. 1250.
[52] A. Kaczor, L.M. Proniewicz, R. Almeida, A. Gómez-Zavaglia, M.L.S. Cristiano, A. M. Matos Beja, et al., J. Mol. Struct. 892 (2008) 343–352.
[53] A. Kaczor, R. Almeida, A. Gómez-Zavaglia, M.d.L.S. Cristiano, R. Fausto, J. Mol. Struct. 876 (2008) 77–85.
[54] F. Weinhold, C.R. Landis, Valency and Bonding: A Natural Bond Orbital Donor-Acceptor Perspective, Cambridge University Press, Cambridge, 2005.
[55] E.D. Glendening, D.M. Hiatt, F. Weinhold, Natural bond orbital analysis of chemical structure, spectroscopy, and reactivity: how it works, in: M. Yáñez, R. J. Boyd (Eds.), Comprehensive Computational Chemistry (First Edition), Elsevier, Oxford, 2024, pp. 406–421.
[56] S. Gumus, T. Sundius, V.T. Yilmaz, Spectrochimica Acta Part A: Mol. Biomol. Spectrosc. 98 (2012) 384–395.
[57] J.S. Murray, P. Politzer, WIREs Comput. Mol. Sci. 7 (2017) e1326.
[58] P.K. Chattaraj, U. Sarkar, D.R. Roy, Chem. Rev. 106 (2006) 2065–2091.
[59] N. Boukabcha, A. Benmohammed, M.H.M. Belhachemi, M. Goudjil, S. Yahiaoui, Y. Megrouss, et al., J. Mol. Struct. 1285 (2023) 135492.
[60] L.R. Domingo, M.J. Aurell, P. Pérez, R. Contreras, Tetrahedron. 58 (2002) 4417–4423.
[61] G. Socrates, Infrared and Raman Characteristic Group Frequencies: Tables and Charts, Wiley, 2004.
[62] A. Alharbi, A.M. Alqahtani, M. Mojally, A.F. Qarah, A.H. Alessa, O.M. Alatawi, et al., J. Mol. Struct. 1305 (2024) 137833.
[63] D.L. Pavia, G.M. Lampman, G.S. Kriz, J.A. Vyvyan, Introduction to spectroscopy, Cengage Learning (2014).
[64] B.H. Stuart, Infrared Spectroscopy: Fundamentals and Applications, Wiley, 2004.
[65] T.S. Xavier, N. Rashid, I. Hubert Joe, Spectrochimica Acta Part A: Mol. Biomol. Spectrosc. 78 (2011) 319–326.
[66] S. Hamamci, V.T. Yilmaz, S. Gumus, O. Büyükgüngör, Struct. Chem. 19 (2008) 123–129.
[67] D.N. Sathyanarayana, Electronic Absorption Spectroscopy and Related Techniques, Universities Press, 2001.
[68] A. Bayazeed, H. Alharbi, A.I. Alalawy, R.B. Alnoman, J. Qurban, A. Alsoliemy, et al., J. Photochem. Photobiol. A: Chem. 450 (2024) 115439.
[69] G. Barone, D. Duca, A. Silvestri, L. Gomez-Paloma, R. Riccio, G. Bifulco, Chem. – Eur. J. 8 (2002) 3240–3245.
[70] J. Smirnovienė, A. Smirnov, A. Zakšauskas, A. Zubrienė, V. Petrauskas, A. Mickevičiūtė, et al., ChemistryOpen. 10 (2021) 567–580.
[71] P. Trivedi, N. Adhikari, S.A. Amin, T. Jha, B. Ghosh, Eur. J. Pharmaceutic. Sci. 124 (2018) 165–181.
[72] H.M. Abumelha, O.M. Alatawi, A.H. Alessa, F.A. Alatawi, A. Bayazeed, N.A. Obaid, et al., J. Mol. Struct. 1309 (2024) 138233.